

Enhanced Oxygen Redox Kinetics and Stability in Li–O₂ Batteries Using Trimetallic MnCo_{2-x}Cu_xO₄ Spinel Catalysts

Pavithra Kannan,^[a] Shivaraju Guddehalli Chandrappa,^[a] Raju Kumar Gupta,^[b] and Annigere S. Prakash*^[a]

High energy density rechargeable Li–O₂ batteries (LOBs) have garnered significant attention as a promising energy storage device. However, the sluggish oxygen redox kinetics impeded the efficiency and cycling performance during both the charge and discharge processes. To address this issue, we introduce a non-noble-trimetallic MnCo_{2-x}Cu_xO₄ (X=0 to 1) spinel interface as a bifunctional catalyst, to improve the reaction kinetics and cycle stability of LOBs. The half-filled e_g orbital improves the synergistic interaction between Cu⁺/Cu²⁺, Co²⁺/Co³⁺, and Mn³⁺/Mn⁴⁺ redox pairs in the lattice, which enhances catalytic performance. In the series of MnCo_{2-x}Cu_xO₄ (X=0 to 1) spinel

catalyst MnCo_{1.75}Cu_{0.25}O₄ (MCU25) emerged as a standout performer. This exhibited notable half-cell performance, featuring superior ORR/OER bifunctional electrocatalytic activity with a ΔE of 1.15 V (vs RHE). Notably, the MCU25 cathode exhibited remarkable stability for over 1250 hours, enduring 225 cycles at 500 mA h g⁻¹ and stable up to 70 cycles at a capacity limit of 1000 mA h g⁻¹ in LOBs. Furthermore, it demonstrated an exceptional discharge-specific capacity of 11272 mA h g⁻¹ at a current density of 175 mA g⁻¹, exceeding the performance achieved by state-of-the-art RuO₂ around 10180 mA h g⁻¹.

Introduction

The rapid and extensive consumption of conventional gasoline and fossil fuels has led to a substantial increase in atmospheric greenhouse gases, thereby causing significant effects on global warming and climate change. Accordingly, exploring alternative avenues for energy storage and conversion becomes imperative; this includes exploring technologies like batteries, supercapacitors, and fuel cells. Among these options, Rechargeable metal-air batteries, with Li, Zn, Al, and other metals, are widely recognized as sustainable and efficient storage devices.^[1,2] Notably, non-aqueous LOBs offer a high specific energy density of around 3500 Wh kg⁻¹, making them the most attractive energy storage device. However, commercialization of LOBs

remains challenging due to their larger overpotential, inadequate cycling stability, and low round trip efficiency, as well as their limited rate performance.^[3,4] The efficiency of LOBs is heavily influenced by the slow redox kinetics of Li₂O₂ formation during discharge and subsequent Li₂O₂ decomposition during charge. The identification of the right catalysts that can improve this rate of both oxygen reduction reaction (ORR) and oxygen evolution reaction (OER) is vital for enhancing the electrochemical performance of LOBs.^[5,6]

Transition metal (TM) oxides,^[7] nitrides,^[8] carbonaceous materials,^[9] phosphides^[10] and perovskites^[11] are widely employed in LOBs as cathode catalysts, which possess effective catalytic performance in ORR/OER reactions. Sr and Fe cation-codoped LaCoO₃ perovskite demonstrate extremely low overpotential, ultrahigh specific capacity, and superior long-term cycling stability.^[6a] Compared to the other materials, spinel oxides stand out as attractive catalysts as they offer the ability to fine-tune their composition and position in the crystal structure and improve oxygen adsorption and desorption capabilities.^[12,13] The spinel structure (AB₂O₄) provides numerous sites for accommodating cations in different valence states due to the presence of both tetrahedrally coordinated A points and octahedrally coordinated B points. Which are linked together by internal corner-sharing A_{Td}–O–B_{Oh} bonds and edge-sharing B_{Oh}–O–B_{Oh} bonds.^[14] Within a spinel lattice, the oxygen anions are shared by four adjacent transition metal cations. Specifically, one cation occupies a tetrahedral interstice, while the other three are situated in octahedral interstices. The covalency of the redox active B_{Oh}–O and A_{Td}–O bonds are determined by the electron polarization from the oxygen anions towards the four closest TMs. which is influenced by the splitting of d orbitals in different geometries.^[15] The occupancy of the B_{Oh} site in the spinel structure is a major factor in enabling strong electronic interactions with molecular oxygen and oxygenated species.^[16]

[a] P. Kannan, S. Guddehalli Chandrappa, A. S. Prakash
Academy of Scientific and Innovative Research (AcSIR), Ghaziabad-201002, India
and
CSIR – Central Electrochemical Research Institute-Chennai Unit, CSIR Madras Complex, Taramani, Chennai-600113, India
E-mail: prakash@cecri.res.in
prakash.as@gmail.com

[b] R. Kumar Gupta
Department of Chemical Engineering, Indian Institute of Technology Kanpur, Kanpur 208016, Uttar Pradesh, India
and
Department of Sustainable Energy Engineering, Indian Institute of Technology Kanpur, Kanpur 208016, Uttar Pradesh, India
and
Kotak School of Sustainability, Indian Institute of Technology Kanpur, Kanpur 208016, Uttar Pradesh, India
and
Chandrakanta Kesavan Centre for Energy Policy and Climate Solutions, Indian Institute of Technology Kanpur, Kanpur 208016, Uttar Pradesh, India
and
Supporting information for this article is available on the WWW under <https://doi.org/10.1002/batt.202400615>

In particular, the electron population within the anti-bonding state is created by the core metal ions and oxygen ions, leading to optimal modulation of the d-band center which promotes the overall redox rate during the reaction. Therefore, varying the cationic position and charge either at the A_{Td} site or neighbouring B_{Oh} site can accelerate the kinetics of the ORR/OER process.^[17,18] This can be achieved by incorporating the partially filled e_g orbital-containing metal ions with high electronegativity.

The flexibility of first-row transition metals in their ionic radius and oxidation states allows them to interact more favourably with oxygen-containing groups, leading to enhanced current density and reduced overpotentials during ORR/OER. Mixed-bimetallic spinel structures based on cobalt (Co), manganese (Mn), iron (Fe), and other metals (e.g., Co_3O_4 , $MnCo_2O_4$, and $NiCo_2O_4$) offer fast electron transfer kinetics in ORR/OER performance, making them highly effective catalysts for LOBs.^[19–21,59] The intrinsic site-specific activity of multivalent cobalt (Co) cations present in the octahedral (Oh) and tetrahedral (Td) coordination significantly enhances the ORR/OER activity and offers extended cycling performance in LOBs. The concurrent occurrence of Co^{3+} and Co^{2+} within the Co_3O_4 spinel promotes O adsorption energy to form OOH^* and deprotonates OOH^* to form O^{2-} . In the Co_3O_4 spinel structure, replacing the A_{Td} site with different metal ions such as ($A=Mn$, Co, Ni, Cu, Zn) with varying electronegativity offers the high affinity of Co ions towards oxygen-containing species.^[22,23] In particular, incorporating Manganese (Mn) with different valence states into Co_3O_4 spinel can enhance its intrinsic ORR/OER performance, resulting in a larger current density.^[24] Since Co-based transition metal oxides have strong OER catalytic activity, while Mn-based transition metal oxides exhibit excellent ORR catalytic activity, this makes the combination of Mn–Co mixed oxides of considerable interest as bifunctional catalysts for LOBs.

To further improve the bifunctional activity of Mn–Co spinel numerous strategies have been employed, such as incorporating heteroatoms, defects, carbon substrates, and heterostructures. Specifically, introducing a foreign-metal cation significantly enriches the catalytic sites or confers new catalytic activity to the catalyst.^[25–27] Copper (Cu) has garnered significant interest in the field of catalysis, due to its remarkable catalytic performance, affordability, and wide range of accessible oxidation states.^[28,29] The incorporation of Cu cation in a mesoporous Co spinel creates a synergistic interaction between Co and Cu cation, leading to an increase in ORR/OER activity.^[30,31] Cu doping in Co_3O_4 spinel increases the Co^{3+} ion content in the octahedral sites through the occupation of Cu in tetrahedral sites. It is established that Co ions with high valence state in octahedral sites are favourable for the oxygen redox process leading to the generation of enriched active sites.^[32–34] The robust electronic interaction enabled by the Cu–O–Co bonds in $CuCo_2O_4$ exhibits excellent bifunctional activity, significantly reduces charge overpotential, and exhibits high specific capacity in LOBs.^[35,36] This mechanistic understanding provides significant guidance toward designing a superior bifunctional active catalyst through cation-tuning. Transition

metal ions possessing a single electron within the octahedrally splintered e_g orbital display remarkable reactivity in both ORR and OER reactions. Our findings reinforce this concept by the existence of Co^{2+} ($t_{2g}^6 e_g^1$) in a low spin state and Mn^{3+} ions ($t_{2g}^3 e_g^1$) in a high spin featuring a single e_g electron within the Mn–Co spinel framework. The presence of this single e_g electron initiates strong Jahn-Teller distortion, causing a deviation from the ideal octahedral arrangement, which in turn weakens the M–OH bonds and promotes O_2 reduction. The combination of metal ions with comparable ionic radius, high electronegativity, and a filled e_g orbital causes fast electron exchange between cations occupying octahedral and tetrahedral sites.

Through the implementation of these strategies, we explored the impact of tuning the electronic structure of the Mn–Co spinel framework by introducing varying ratios of Cu (0, 0.25, 0.5, 0.75, and 1) at the Co site. The inclusion of copper enhances the efficiency of the four-electron oxygen reduction process by promoting improved O–O bond stretching and creating favorable adsorption energies for O_2 and OOH .^[37] Additionally, the existence of Cu^+/Cu^{2+} ion pairs led to variations in the occupancy and ratio of the $Co^{2+/3+}$ and $Mn^{3+/4+}$ redox pairs in the trimetallic $MnCo_{2-x}Cu_xO_4$ spinel. This, in turn, induces robust synergistic effects between the ion pairs.^[38] This cooperative interplay of trimetallic surface significantly governs the intrinsic adsorption behaviour of Li_2O_2 intermediates with a unique morphology. Facilitating the formation of Li_2O_2 intermediate during discharge (ORR) and its decomposition during charge (OER), which ultimately results in optimized performance. Evaluations of half-cell performance were executed to assess bifunctionality, offering deeper insights into the efficacy of the $MnCo_{2-x}Cu_xO_4$ catalysts. Among the prepared compositions $MnCo_{1.75}Cu_{0.25}O_4$ excels with the remarkable bifunctional activity of 1.15 V, proving effective performance in aqueous environments as well as in a non-aqueous homemade LOB. Which exhibited exceptional charge-discharge stability over a notable span of 225 cycles, while adhering to the specified capacity limit of 500 $mA\cdot h^{-1}$ with low overpotential.

Results and Discussion

The Cu-substituted trimetallic spinel framework was synthesized through a simple low-temperature solution combustion method. The X-ray diffractogram indicates a recognizable pattern that matches with MCO ($MnCo_2O_4$ JCPDS - 023-1237), as depicted in Figure S1. Further, Figure 1a compares the XRD patterns of the prepared compositions to that of MCO spinel. This demonstrates that the spinel structure is retained with different amounts of Cu substitution on Co place. By increasing Cu doping in the spinel, the diffraction peak corresponding to the (311) plane shifts towards higher angles as shown in Figure 1b.

Beyond a certain threshold level, an increase in Cu concentration leads to the replacement of Co from the octahedral position by Cu^{2+} ions. Which induces the lattice distortion, thereby causing the characteristic peak shift.^[39,40] The

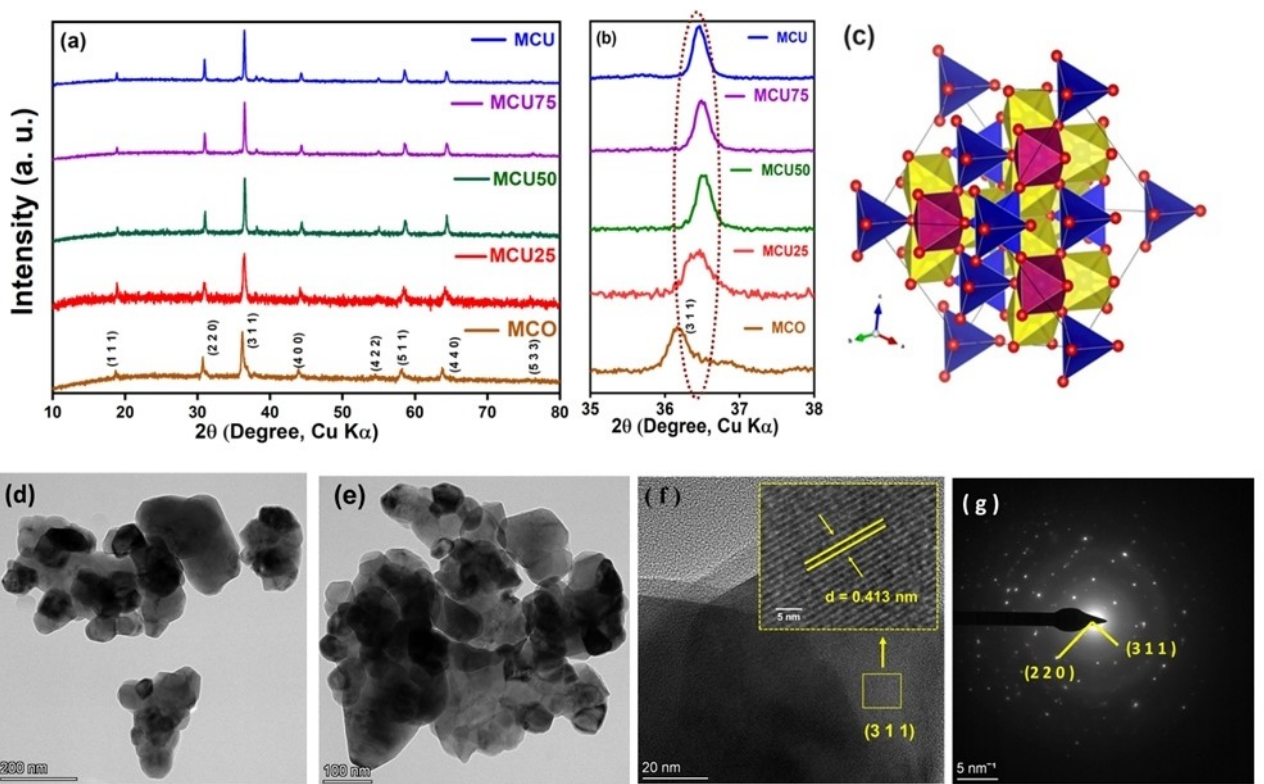


Figure 1. (a) Powder XRD patterns of the prepared trimetallic $\text{MnCo}_{2-x}\text{Cu}_x\text{O}_4$ ($X=0, 0.25, 0.5, 0.75$ and 1) spinel. (b) XRD peak shift corresponding to $(3,1,1)$ plane with different Cu content in the angle of between 35 to 38° . (c) 3D framework highlighting the trimetallic spinel lattice. (d),(e) High-resolution TEM images of the MCU25 catalyst (f) HR-TEM images of the $(3\ 1\ 1)$ crystal plane with d spacing (g) SAED patterns with planes $(3\ 1\ 1)$ and $(2\ 2\ 0)$.

average crystalline size of the spinel compositions was determined from their primary diffraction peaks using the Scherrer equation. This analysis unveils a growth of the average crystal size corresponding to varying Cu concentrations. All these details provided in Table S1, which include lattice constants and d -spacing values, are acquired through the application of Bragg's law.

The Rietveld refined XRD profiles of MCU, MCU75, MCU50, and MCU25 fitted well with the observed X-ray data as shown in Figure S2 (a-d). This illustrates that the compound adopts a cubic phase with an $\text{Fd}-3\ \text{m}$ space group. The lattice parameter varies from $8.14 \pm 0.004\ \text{\AA}$ to $8.19 \pm 0.002\ \text{\AA}$ with varying Cu-concentration. Since Cu^{2+} ($3\text{d}^9 - \text{t}_{2g}^6\text{e}_g^3$) with a vacant e_g orbital possesses strong John Teller distortion and the highest affinity to occupy an octahedral (Oh) site replaces Co atoms from the Oh site.^[33] The variation in the lattice parameter is due to the replacement of the Co^{2+} cation with the Cu^{2+} cation in the Oh site of MCO. The ionic radii of high-spin Cu^{2+} are slightly less than that of octahedral Co^{2+} hence the lattice parameter experiences a slight decrease. The atomic positions, lattice parameters, occupancy, and other structural parameters affected by increasing Cu concentration are summarized in Table S2. The occupancy factors derived from the refinement data indicate that Cu primarily occupies the octahedral-B site of the spinel structure. Figure S3 (a-d) displays FE-SEM images of the spinel catalyst, indicating the existence of well compact microstructure with distinctive morphology. The magnified SEM

image further revealed that the surface of these particles had a highly agglomerated hierarchical structure with irregularly arranged grains. Furthermore, as the Cu doping content increased, the surface grains of MCU particles exhibited a significant enlargement compared to MCU25. Figures 1d and e displays an HR-TEM micrograph of the $\text{MnCo}_{0.75}\text{Cu}_{0.25}\text{O}_4$ sample, the micrographs and the electron diffraction pattern indicate highly crystalline particles. The catalyst exhibits non-spherical shapes with a size ranging between 20 – $40\ \text{nm}$ and is notably agglomerated. Figure 1f exhibits clear lattice fringes within the grains, showcasing interplanar spacing of $0.413\ \text{nm}$ aligns with the $(3\ 1\ 1)$ plane. The selected area electron diffraction (SAED) pattern in Figure 1g reveals bright spots that confirm the presence of (311) and (220) planes, indicating the cubic phase of the material.

To investigate the chemical state of Cu, Mn, and Co in the XPS spectrum, the binding energy of core-level electrons was utilized after an elemental survey (Figure S4) that confirmed the presence of these elements. Figure 2a depicts the $\text{Co}\ 2\text{p}$ spectrum of $\text{MnCo}_{2-x}\text{Cu}_x\text{O}_4$ ($X=0.25, 0.5, 0.75$ and 1) catalyst series with two spin-orbit peaks ($\text{Co}\ 2\text{p}_{1/2}$ and $\text{Co}\ 2\text{p}_{3/2}$), Conforming the Co^{3+} (779.3 and $795.1\ \text{eV}$) and Co^{2+} (781.5 and $796.6\ \text{eV}$), respectively. The presence of two shakeup satellites located at 786.35 and $803.4\ \text{eV}$, with an energy gap of $\approx 6\ \text{eV}$ between the main Co peak and satellite peaks, indicates the 2^+ -valence states, while values associated with ≈ 9 – $10\ \text{eV}$ indicate the 3^+ -valence states.^[19,38,41] The analysis revealed that the ratio

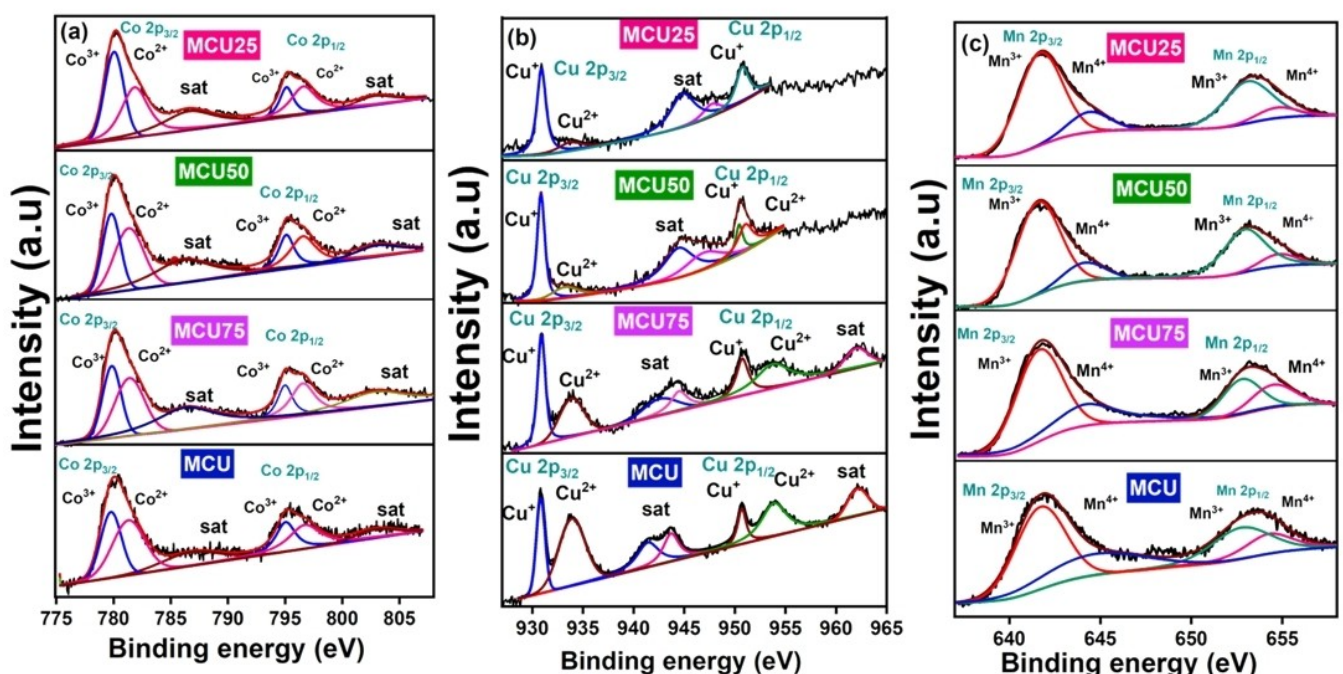


Figure 2. High-resolution XPS spectra of the trimetallic $\text{MnCo}_{2-x}\text{Cu}_x\text{O}_4$ ($X = 0.25, 0.5, 0.75$ and 1) spinel catalyst. Deconvoluted peaks of (a) Co 2p spectrum between 775–805 eV binding energy. (b) Cu 2p spectrum between 930–965 eV. (c) Mn 2p spectrum between 640–660 eV.

of $\text{Co}^{2+}/\text{Co}^{3+}$ exhibited a positive correlation with the increasing Cu content, as listed in Table 1 through peak area integration. This table provides the overall relative number of different ions present in synthesized spinel composition and suggests a representative formula for their ionic distribution.

At higher copper loadings (MCU and MCU75), the Cu 2p spectra show distinct peaks at 931.1 eV and 933.9 eV, corresponding to $\text{Cu } 2\text{p}_{1/2}$ and $\text{Cu } 2\text{p}_{3/2}$ ^[42] with satellite peaks at 962 eV and 942 eV indicating Cu^+ and Cu^{2+} states^[31,43,44]. As the Cu loading decreases in MCU50 and MCU25, Cu^+ becomes dominant, leading to a significant drop in the intensities of both the satellite and Cu^{2+} peaks, as depicted in Figure 2b.

Notably, monovalent copper ions occupy tetrahedral voids, while bivalent copper ions occupy octahedral voids in the spinel phase. The XPS data suggests that a decrease in the Cu content of the spinel structure results in a higher concentration of Co^{3+} ions. The broad Mn 2p_{3/2} and Mn 2p_{1/2} peaks were resolved into four subpeaks^[45] with binding energies corresponding to Mn^{3+} (641.4 and 654.2 eV) and Mn^{4+} (644.12 and 654.8 eV), as illustrated in Figure 2c. The relative amount of

different Co, Mn, and Cu species in the spinel were detailedly listed in Table S3 (a–c). In the O-1 s spectrum, three distinguishable photoelectron peaks were observed, corresponding to lattice oxygen within the spinel structure, oxygen originating from hydroxide ions, and oxygen derived from physically adsorbed water molecules. The N_2 adsorption-desorption isotherm and pore size distribution of catalysts with different compositions are depicted in Figure S5 (a–d). The surface area values for various catalyst compositions are listed in Table S4. The variations in surface area values among different compositions are negligible. The catalysts displayed a type II behaviour in the isotherm hysteresis curve, indicating the presence of mesoporous structures that emerged under varying relative pressure conditions.^[46] Furthermore, the pore size distribution of the catalysts was analyzed with a Barret-Joyner Halenda (BJH) model, and the curve is illustrated in the Figure. These data suggest that the catalytic activity is influenced by the site occupancy of Co, Mn, and Cu cations on the spinel surface.

Table 1. The relative intensity ratio of cations in the spinel compositions and their ionic distribution derived from the XPS data.

Sample	$\text{Co}^{2+}/\text{Co}^{3+}$ Ratio	$\text{Mn}^{3+}/\text{Mn}^{4+}$ Ratio	$\text{Cu}^+/\text{Cu}^{2+}$ Ratio	Formula
MCU25	0.96	3.91	3.80	$(\text{Cu}^{+}_{0.20}\text{Cu}^{2+}_{0.05})(\text{Mn}^{+3}_{0.73}\text{Mn}^{+4}_{0.27})(\text{Co}^{+2}_{0.85}\text{Co}^{+3}_{0.92})\text{O}_4$
MCU50	1.26	5.48	2.7	$(\text{Cu}^{+}_{0.35}\text{Cu}^{2+}_{0.15})(\text{Mn}^{+3}_{0.63}\text{Mn}^{+4}_{0.37})(\text{Co}^{+2}_{0.83}\text{Co}^{+3}_{0.67})\text{O}_4$
MCU75	1.269	2.119	1.15	$(\text{Cu}^{+}_{0.4}\text{Cu}^{2+}_{0.35})(\text{Mn}^{+3}_{0.66}\text{Mn}^{+4}_{0.34})(\text{Co}^{+2}_{0.96}\text{Co}^{+3}_{0.54})\text{O}_4$
MCU	1.34	1.90	0.47	$(\text{Cu}^{+}_{0.32}\text{Cu}^{2+}_{0.68})(\text{Mn}^{+3}_{0.48}\text{Mn}^{+4}_{0.52})(\text{Co}^{+2}_{0.71}\text{Co}^{+3}_{0.29})\text{O}_4$

Electrochemical Performance

Electrocatalytic half-cell performance of the synthesized samples towards the oxygen evaluation reaction (OER) was assessed by conducting linear sweep voltammetry (LSV) in 1 M KOH solutions and the results are shown in Figure 3a. Further, to understand the electrochemical kinetics of the material during the OER process, Tafel plots (Figure 3b) are plotted, which correlate the logarithm of current density (J_k) against the overpotential ($\eta = V - 1.23$ V vs RHE). The polarization curves indicated the MCU25 catalyst demonstrates superior OER activity, showcasing a prior onset potential of 1.44 V and a high overpotential of 217 mV dec⁻¹. Thus, the OER activity of the MCU25 catalyst surpasses those of $MnCo_{2-x}Cu_xO_4$ ($x=0.5, 0.75$ and 1) compositions and state-of-the-art RuO_2 catalysts. The impressive OER proficiency displayed by MCU25 is attributed to the synergistic effect of Co^{3+}_{oh} and Cu. Generally, within the spinel structure, oxygen ions are surrounded by four transition metal ions, with three metal ions situated in octahedral positions, while the fourth occupies a tetrahedral position. In a tetrahedral site, the metal ion interacts weakly with the oxygen p-orbitals through side-to-side overlap. But, in an octahedral site, the metal ion engages a robust s interaction with direct head-on overlap.^[14,15] The comparable ionic radius and high electronegativity of Cu ions with Co-ions in MCU25 facilitates higher concentrations of Co^{3+} ions to occupy the octahedral site.^[36,47] Further, substituting high electronegative Cu ions leads to increased polarization of oxygen towards tetrahedral Cu cations and also replaces octahedral Co cations. The lowering of Co^{3+} ions concentration from 0.92 to 0.23 was evidenced by the data derived from XPS as depicted in Table 1. Progressively

improved covalency of the Co–O bond was further evidenced by the OER overpotential, which increased from 121 mV dec⁻¹ to 217 mV dec⁻¹ with varying Cu content.

The oxygen reduction (ORR) capability of the catalyst was assessed by conducting Cyclic voltammogram (CV) plots in both N_2 -saturated and O_2 -saturated 0.1 M KOH solutions at a scan rate of 10 mVs⁻¹. Further to understand the charge transfer characteristics of the trimetallic $MnCo_{2-x}Cu_xO_4$ ($X=0.25$ to 1), LSV measurements were conducted at various rotating speeds, as depicted in Figure S6. It is evident that the current density of the catalyst progressively increases with an increase in rotation speed. This can be attributed to the accelerated oxygen transport and reduced diffusion path on the electrode surface.^[48] Using the Koutecky–Levich (K-L) equation the electron transfer number and kinetic current density across the potential range of 0.2–0.8 V are calculated. Among all the $MnCo_{2-x}Cu_xO_4$ compositions, MCU25 outperforms benchmark 40 wt % Pt/C with superior current density at a sweep rate of 2 mVs⁻¹ in LSV measurements at 1600 rpm, as shown in Figure 3c. Additionally, it demonstrates nearly 100% selectivity for 4e– electron transfer in the ORR process compared to the other compositions, as illustrated in Figure 3e. This superior ORR performance of MCU25 is attributed to the electron exchange interactions between the edge-sharing Mn_{oh} –O– Co_{oh} . The higher concentration of Co^{3+} ions in octahedral sites promotes an internal redox process, ($Co^{3+} + Mn^{3+} \rightarrow Co^{2+} + Mn^{4+}$) that gradually alters the e_g occupancy of Mn cations.^[16] Transition metal ions that possess a single electron in the octahedrally distributed d-orbitals (e_g level) are notably ORR active.^[24,49] One e_g electron in σ^* orbital cause the destabilization of the M–OH²⁺ bond, thereby facilitating the intermediate

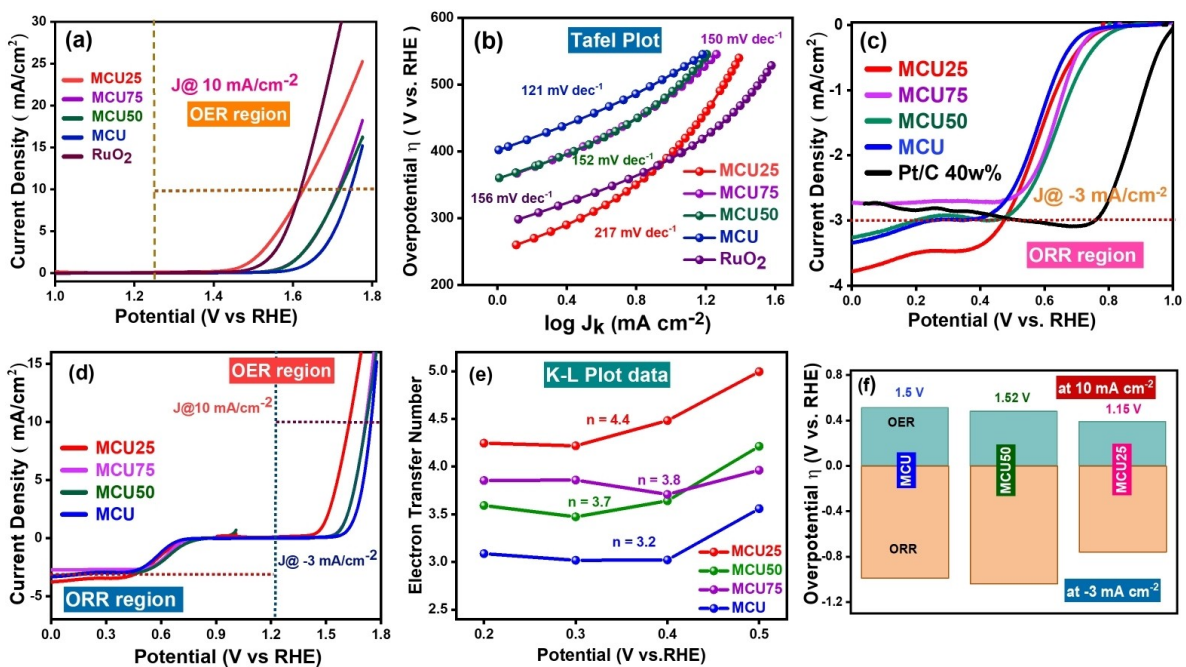


Figure 3. Bifunctional ORR/OER activities of trimetallic spinel (a) OER activity-LSV curves of $MnCo_{2-x}Cu_xO_4$ ($X=0.25, 0.5, 0.75$ and 1) and RuO_2 catalyst at a sweep rate of 2 mVs⁻¹ (b) Corresponding OER-Tafel plots. (c) ORR activity-LSV curves of $MnCo_{2-x}Cu_xO_4$ ($X=0.25, 0.5, 0.75$ and 1) and 40 wt % Pt/C recorded at 1600 rpm. (d) Comparison of the bi-functional activities of $MnCo_{2-x}Cu_xO_4$ ($X=0.25, 0.5, 0.75$ and 1) catalyst. (e) Electron transfer number at different Potentials comparison for each catalyst. (f) ORR and OER bifunctional overpotential comparison plot

reaction between O_2^{2-}/OH^- . This strong John Teller distortion caused by the Mn^{3+} (high spin $t_{2g}^3e_g^1$) and Co^{2+} (low spin $t_{2g}^6e_g^1$) cation weakens the M–OH bond and facilitates the of O_2 reduction.^[50]

To evaluate the bifunctional activity of the trimetallic spinel, we utilized the potential difference (ΔE) between OER half-wave potential and ORR potential at benchmark current densities (ORR = -3 mA cm⁻² and OER = 10 mA cm⁻²) as depicted in Figure 3d and the corresponding results are summarized in Table 2. Within the $MnCo_{2-x}Cu_xO_4$ series, MCU25 displayed superior bifunctional activity ($\Delta E = 1.15$ V), as evidenced by the overpotential difference observed in Figure 3f for OER/ORR activities. The combined synergistic interaction achieved by Co–O–Cu and Mn–O–Co cations in the spinel lattice, contributing to the highest bifunctional activity of MCU25, aligns well with the preceding discussions. This prompts further exploration of these catalysts for potential applications.

Li–O₂ Battery Performance

The electrocatalytic efficiency of the trimetallic $MnCo_{2-x}Cu_xO_4$ spinel was tested as an air cathode in a Li–O₂ cell using a 1 M LiTFSI in TEGDME non-aqueous electrolyte. For all experiments, the average mass loading of active materials on the GDL surface was consistently maintained between 0.35–0.45 mg cm⁻². Using metallic lithium as a reference/counter electrode, the typical CV curve of the Li–O₂ cell was recorded at a scan rate of 5 mV s⁻¹ with a voltage window of 2.0–4.5 V. Figure 4a and Figure S7 depicts the comparison of CV profiles of the prepared $MnCo_{2-x}Cu_xO_4$ (X = 0, 0.25, 0.5, 0.75 and 1) spinel compositions with Ketjen Block (KB) carbon and benchmark RuO₂. Among these MCU25 exhibited the most prominent oxidation and reduction peaks. In particular, it shows an ORR cathodic plateau at approximately 2.57 V, which indicates the formation of Li_2O_2 ($O_2 + 2Li^+ + 2e^- \rightarrow Li_2O_2$).^[51] Similarly, an anodic OER plateau at around 3.2 V was observed, attributed to the decomposition of Li_2O_2 ($Li_2O_2 \rightarrow O_2 + 2Li^+ + 2e^-$).^[52] The prior onset potential and elevated peak current density associated with the MCU25 cathode signify an enhanced formation and decomposition of Li_2O_2 .

The Electrochemical Impedance Spectroscopy (EIS) measurements with all synthesized samples were conducted, as illustrated in Figure 4c. The Nyquist plots were fitted using an R1(Q1R2)(Q2R3)W equivalent circuit, and the findings are

detailed in Figure S11 & Table S6. In this model, R1 represents the solution resistance, while R2 reflects the resistance at the solid electrolyte interface, which forms due to side reactions at the electrode-electrolyte interface. R3 corresponds to the charge transfer resistance, and W (Warburg Impedance) is related to the mass transfer of oxygen (O_2) at the cathode catalyst. These results indicate that the MCU25 cathode exhibits significantly lower resistance values than other cathodes, suggesting superior electronic conductivity that facilitates faster and more efficient electron transfer during battery operation.

Galvanostatic charge-discharge experiments were performed using a Swagelok Li–O₂ cell with a voltage window ranging from 2 to 4.5 V at a current density of 175 mA g⁻¹ as illustrated in Figure 4b. The MCU25 cathode significantly exhibited much higher full discharge/charge capacity of 11272 mA h g⁻¹ in comparison with the other MCO (6594 mA h g⁻¹), MCU25 (11272 mA h g⁻¹), MCU50 (8650 mA h g⁻¹), MCU75 (8802 mA h g⁻¹), MCU (6850 mA h g⁻¹) and RuO₂ (10180 mA h g⁻¹). It is to be noted here that the XPS analysis discussed previously, which indicated MCU25 catalyst having higher ratios of Cu^{+}/Cu^{2+} , Co^{2+}/Co^{3+} , and Mn^{3+}/Mn^{4+} , aligns well with its improved performance. Specifically, the presence of Mn^{3+}/Mn^{4+} in Li–O₂ cells facilitates the de-lithiation process of Li_2O_2 , forming LiO_2 intermediates that readily decompose to generate O_2^{51} . The Co^{2+}/Co^{3+} redox couple reduces ORR overpotential by interacting with superoxide and Li_2O_2 , and Co^{3+} also controls Li_2O_2 size to enhance charging efficiency.^[53,54] Incorporating high electronegative Cu centers improves electron conductivity and lowers adsorption strength towards Li–O intermediates, thereby reducing the reaction energy barrier in LOBs.^[30,55,56] The high synergistic combination of these redox pairs within the MCU25 catalyst renders it superior for LOBs.

The remarkably high specific capacity and reduced overpotential of MCU25 spinel garnered substantial interest in exploring its stability. Figure 4(e–f) presents the full charge-discharge profile of the MCU25 and RuO₂ catalyst in Li–O₂ cells without capacity limitation at a current density of 175 mA h g⁻¹. The specific capacity of both catalysts is comparable in the initial cycles, and their stability is retained up to the sixth cycle. However, the overpotential observed for MCU25 is significantly lower than that of the state-of-the-art RuO₂ catalyst. Additionally, the specific capacity assessed at the end of the sixth cycle for MCU25 is higher than that of RuO₂. These findings indicate the ability of MCU25 to mediate discharge product formation

Table 2. Summary of half-cell bifunctional testing results for the spinel catalyst.

Catalyst	OER performance		ORR performance	
	E(V) @ i = 10 mA/cm ²	i _{max} (mA/cm ²) @E = 1.8 V vs RHE	E(V) @ i = -3 mA/cm ²	i _{max} (mA/cm ²) @E = 0.2 V vs RHE
MCU25	1.62	25.3	0.47	-3.4
MCU50	1.71	16.3	0.19	-2.99
MCU75	1.71	18.3	-	-2.7
MCU	1.74	15.1	0.24	-3.05

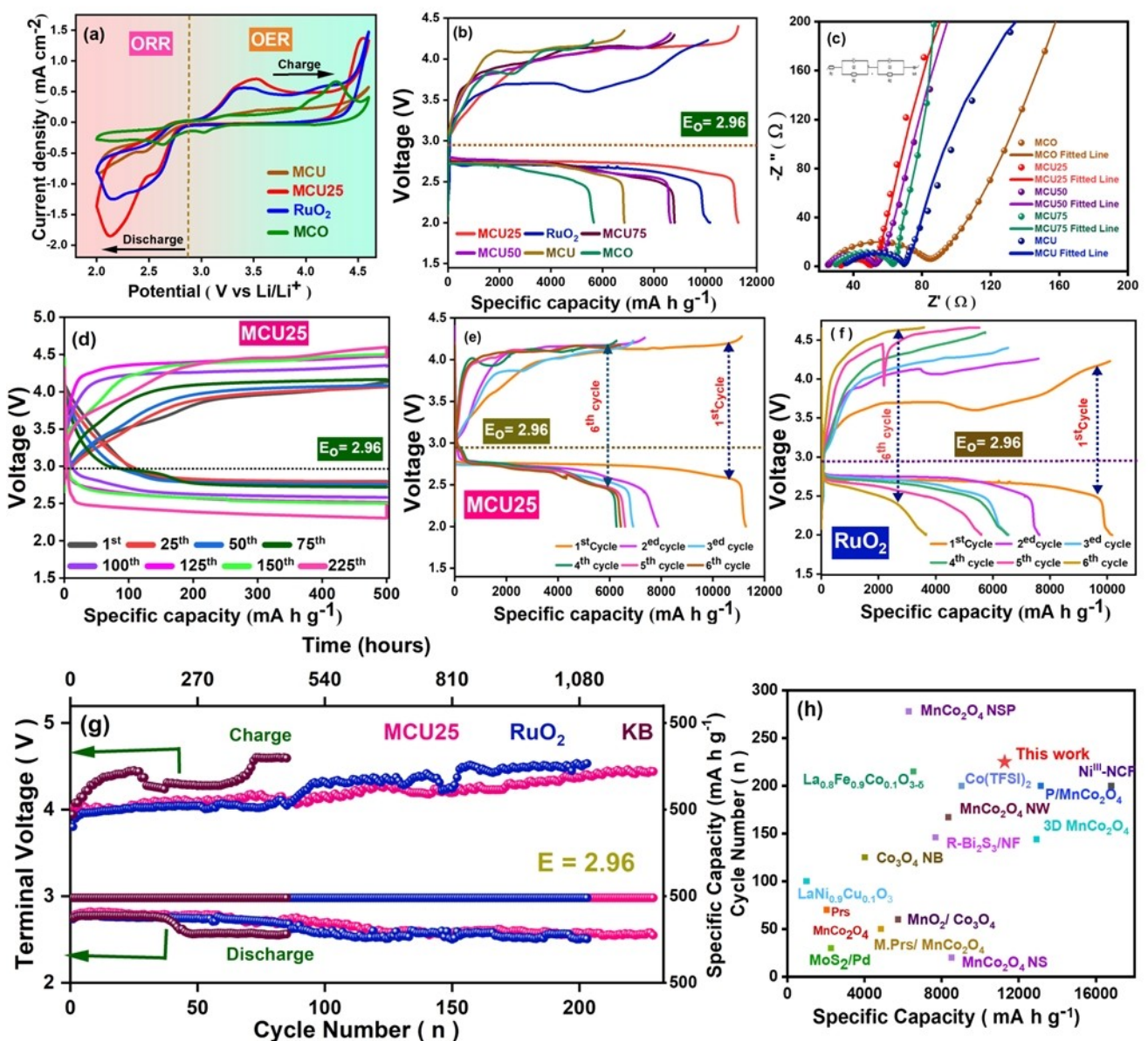


Figure 4. Li-O₂ battery performance (a) Cyclic voltammetry curves of MCO.MCU MCU25, and RuO₂ at a scan rate of 5 mV S⁻¹ and the voltage window of 2.0–4.5 V. (b) Comparison of full charge/discharge profile for trimetallic MnCo_{2-x}Cu_xO₄ (X = 0, 0.25, 0.5, 0.75 and 1) and RuO₂ at a current density of 175 mA g⁻¹ (c) Nyquist plots for the synthesized samples (d) The charge/discharge cyclic stability data at Cut off capacity 500 mAh g⁻¹ for MCU25 (e) Galvanostatic full charge discharge curves of (e) MCU25 and (f) RuO₂ at a scan rate of 5 mV S⁻¹ and voltage window of 2.0–4.5 V (g) The terminal discharge/charge voltage of MCU25, RuO₂ and KB cathodes with a restricted capacity of 500 mAh g⁻¹. (h) Literature comparison

and decomposition throughout multiple cycles efficiently. Further, as shown in Figure 4d and Figure S8, the MCU25 catalyst exhibited superior long-cycling stability for 1250 hours, running over 225 cycles with a restricted capacity of 500 mAh g^{-1} , and 70 cycles with a restricted capacity of 1000 mAh g^{-1} at a current density of 175 mA g^{-1} . The terminal discharge/charge voltages of MCU25 catalyst compared with RuO₂ and KB carbon indicate superior cycling stability with a lower overpotential in Figure 4g. As listed in Table S5, and Figure 4h MCU25 catalyst exhibits a high specific capacity and cycling stability compared to the previously reported transition metal-based catalyst.

To understand the underlying mechanism of Li_2O_2 nucleation and growth using these metal oxide catalysts, charge/discharge experiments were conducted at different current densities. Figure S9 shows the rate capability test for the MCU25 catalyst performed with a cut-off capacity of 2000 mAh g^{-1} . Distinct overpotentials of 1.63 V, 1.73 V, 1.88 V, and 1.79 V were observed in the first cycle by varying the current densities to 175, 350, 700, and 1400 mA g^{-1} respectively. This observation emphasizes the superior performance of the MCU25 cathode in terms of lithium storage capacity, cycling stability, and polarization of Li_2O_2 , then the other catalysts.

Ex Situ Study After Discharge and Charge

The reaction sequence during the charge/discharge process with the MCU25 spinel catalyst was investigated by Ex-situ XRD and FE SEM analysis. Figure 5j depicts an XRD pattern for the pristine, discharged, and charged cathode with the comparison of commercial Li_2O_2 . The discharged cathode exhibits discernible peaks at 2θ values of 32.9° , and 35.0° indicating the presence of the Li_2O_2 phase.^[57] However, due to the high crystallinity of carbon peaks from KB carbon and PVDF in the sample, the intensity of Li_2O_2 diffraction peaks was notably low.

Remarkably, these reflections are completely absent in the charged cathode, indicating a reversible process of formation and decomposition of Li_2O_2 during cycling.^[58] To gain insights into the mechanisms driving the polarization curves, EIS measurements were carried out during the charge-discharge cycling of the lithium-oxygen battery (LOB). Figure 5k displays Nyquist plots at three representative stages, before cycling, after discharge, and in the fully charged state of the MCU25 cathode. The equivalent circuit fits are made using the Biologic software, and the proposed equivalent circuit model is represented In Figure S11 and the corresponding values are listed in Table S6. Where the smaller R3 value before cycling denotes the good electronic conductivity of $\text{Li}-\text{O}_2$ cell with MCU25 cathode. Then this is increased to 561.6 ohm for the discharged state and was attributed to an accumulation of the insulating Li_2O_2 discharge product on the surface of the electrode. Further, in a charged state, the R3 value decreased to 229.8. ohm which can be attributed to the reversible formation and decomposition of the Li_2O_2 discharge product. Thus, improving the reversibility of the O_2 electrode.

Furthermore, the shape of transient intermediates formed during the operation of $\text{Li}-\text{O}_2$ batteries was studied using Ex situ FE-SEM analysis. Figure 5(d-f) revealed the presence of Li_2O_2 particles in the discharged state between 5 μm to 500 nm. These particles had a unique morphology, with half-grown hollow trapezoids of tiny Li_2O_2 molecules. However, these particles are absent in the charged state (Figure 5(g-i)). In addition, the distribution of Li_2O_2 was confirmed by elemental mapping (Figure S10) at a resolution of 500 nm. This revealed a clear enrichment of oxygen in the discharged state, with a distinct boundary for Li_2O_2 .

Conclusions

Cation-tuned $\text{MnCo}_{2-x}\text{Cu}_x\text{O}_4$ ($X=0$ to 1) spinel's have evolved as a new class of bifunctional cathode materials for $\text{Li}-\text{O}_2$ batteries, with exceptional OER and ORR activities. This Cu substitution tailors' superior redox properties by facilitating rapid electron transfer within the Mn–O–Co bond, as evidenced by a high electron transfer number (K–L plot) and elevated kinetic current density. The catalyst's enhanced half-cell efficiency is mainly attributed to the elevated concentration of $\text{Cu}^{+}/\text{Cu}^{2+}$, $\text{Co}^{2+}/\text{Co}^{3+}$, and $\text{Mn}^{3+}/\text{Mn}^{4+}$ on the active sites. This interaction expedites the absorption and desorption of OOH^* intermediates, consequently enhancing the charge transfer kinetics for both ORR and OER. Among the various compositions, the $\text{MnCo}_{1.75}\text{Cu}_{0.25}\text{O}_4$ catalyst stands out with high bifunctional activity with low overpotentials, attributed to its high concentration of redox pairs. With this, a prototype $\text{Li}-\text{O}_2$ cell, demonstrates a significantly higher discharge specific capacity

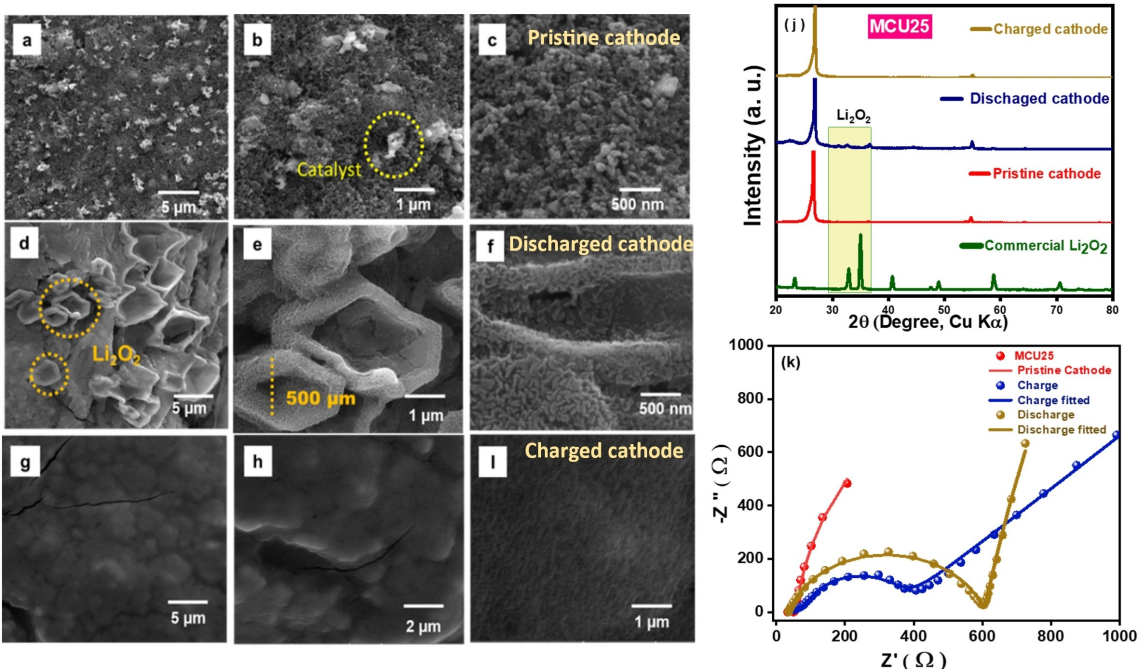


Figure 5. Ex-situ FE SEM images of the MCU25 Cathode in three different states: (a, b, c) pristine, (d, e, f) discharge, and (g, h, i) charge state, each captured at varying magnifications. (j) Ex-situ XRD data for Pristine, charged and discharged cathode in comparison with Li_2O_2 . (k) Fitted impedance spectra (Nyquist Plots) with the corresponding circuit diagram of the MCU25 cathode containing $\text{Li}-\text{O}_2$ cells before cycling, after discharge, and in the charged state.

of $\sim 11272 \text{ mAh g}^{-1}$ and long-term cycling stability over 1250 hours, reaching up to 225 cycles with a restricted capacity of 500 mAh g^{-1} . These results suggest that creating a synergistic effect through cation tuning in spinel cathodes can significantly induce the electrocatalytic properties and improve the performance of the Li–O₂ battery, exceeding that of both bimetallic MnCo₂O₄ and noble metal catalysts. This advanced approach for boosting Li–O₂ battery performance paves the way for exploring trimetallic alternatives to noble metal-based catalysts.

Experimental Section

Synthesis of Non-Noble-Trimetallic MnCo_{2-x}Cu_xO₄ (X = 0 to 1) Spinel

The trimetallic spinel catalysts tailored with Cu substitution were synthesized using a low-temperature solution combustion method. The synthesis began by preparing a precursor mixture consisting of cobalt nitrate hexahydrate (SRL, 97%), manganese nitrate tetrahydrate (Alfa Aesar, 98%), and copper nitrate trihydrate (SRL, 99.5%). These metal nitrates were dissolved in deionized (DI) water at stoichiometric molar ratios. To this solution, oxalyl dihydrazide (Sigma-Aldrich, 98%), serving as the fuel for the combustion, was added. The mixture was stirred at 50°C for about 10 minutes to ensure complete dissolution and uniform distribution of the metal precursors and fuel. The resulting solution was then transferred into a muffle furnace preheated to 350°C, where it underwent dehydration and an exothermic combustion reaction. This process led to the formation of a foamy, homogeneous residue in just 5 minutes. The residue was subsequently ground to ensure uniformity and to break up any agglomerates. Finally, the ground product was calcined at 650°C for 1 hour to further refine the catalyst structure, enhance its stability. The prepared spinel catalysts such as MnCo₂O₄, MnCo_{1.75}Cu_{0.25}O₄, MnCo_{1.5}Cu_{0.5}O₄, MnCo_{1.25}Cu_{0.75}O₄ and MnCoCuO₄ compositions, denoted as MCO, MCU25, MCU50, MCU75 and MCU.

Characterization of Materials

To investigate the crystalline structure and phase purity of the catalyst materials, X-ray diffraction (XRD) analysis was conducted utilizing a Bruker D8 Advance Da Vinci diffractometer operated at 40 kV and 30 mA with Cu K α ($\lambda = 1.418 \text{ \AA}$) radiation. The surface morphology and composition of the catalysts were examined using a MIRA3 TESCAN field-emission scanning electron microscope (FE-SEM). High-resolution transmission electron microscopy (HR-TEM) imaging was performed with the Thermo Scientific Talos F200S. The elemental mapping of the NMATSO was obtained by Bruker energy-dispersive X-ray spectroscopy (EDX) attached to HR-TEM. The determination of specific surface areas was carried out using the Brunauer–Emmett–Teller (BET) method based on the N₂ adsorption/desorption isotherm. To determine the chemical states of metal ions, X-ray photoelectron spectroscopy (XPS) was carried out with a Thermo Fischer XPS spectrometer equipped with an Al K Alpha (1486.7 eV) source.

Electrochemical Measurements

The electrochemical performance of the catalysts was investigated with a rotating disk electrode (RDE) in a PINE RDE setup (Biologic, VSP/VMP 3B-20, France), where a glassy carbon (GC) electrode with a diameter of 5 mm (0.196 cm², PINE) was used as the working

electrode. A Pt wire as the counter electrode and Hg/HgO (1 M KOH) was used as the reference electrode. For the preparation of the catalyst ink, 14 mg of catalyst and 4 mg of Super P carbon were combined with 100 μl of Nafion ionomer (5 wt %, Sigma Aldrich), 600 μl of Isopropanol (Sigma Aldrich), and 300 μl of milli-Q water (mQ) mixed. The GC electrode was coated with the dispersed catalyst ink, utilizing a volume of 5 μl , and achieving a loading of 0.35 mg cm⁻² for all measurements involving samples and reference materials to ensure consistency. The polarization curves for the ORR reaction were recorded at a scan rate of 2 mVs⁻¹ in a 0.1 M KOH (Sigma Aldrich) electrolyte, which was saturated with both O₂ and N₂ gases. The OER polarization curves were measured in a 1 M KOH solution with a sweep rate of 2 mVs⁻¹. The potentials recorded in each experiment, referenced to Hg/HgO, were normalized to the Reversible Hydrogen Electrode using the below equation.

$$E_{\text{RHE}} = E_{\text{Hg/HgO}} + 0.059 \text{ pH} + 0.198 \text{ V}$$

Where E_{RHE} represents the potential vs. RHE, E_{Hg/HgO} denotes the potential vs. Hg/HgO electrode, and pH symbolizes the pH value of the electrolyte.

Preparation of the Air Cathodes and Li–O₂ Cell Assembly

Homemade Swagelok-type cells were employed to assemble Li–O₂ cells within an argon-filled Glovebox, where the O₂ and H₂O content was lower than 0.1 ppm. Li metal foil with an 8 mm diameter (Alfa Aesar) was used as the counter electrode, while a glass fiber membrane (Whatman) served as the separator. The oxygen cathodes were fabricated by coating a catalyst slurry onto a gas diffusion layer (GDL, SGL Carbon – GDL 38 BC). The slurry comprised of active material, Ketjen Block (AkzoNobel) (KB) and PVDF (Sigma Aldrich) poly (vinylidene difluoride) dispersed in N-methyl 2-pyrrolidone (NMP) (Sigma Aldrich) in a proportion of 60:30:10. Afterward, the cathode was dried at 70°C for 24 hours in a vacuum oven to remove residual solvent and cut into a 10 mm diameter. A typical total loading weight of the cathode material on an active area of 1 cm² was approximately 0.30–0.35 mg cm⁻². The current density and specific capacity of the cathode were calculated using the mass of the cathode catalyst. 1 M lithium bis (trifluoro methane sulphonamide) (Sigma Aldrich) in tetra ethylene glycol dimethyl ether (Sigma Aldrich) was used as an electrolyte in LOBs. For the cell reaction highly pure oxygen (99.99% purity) (INDO GAS) was supplied at the pressure of 1 bar from the cathode direction.

Acknowledgements

The authors gratefully acknowledge financial support from the Department of Science and Technology, New Delhi, India, DST/NM/TUE/EE-03/2019-1C-CECRI; Science and Engineering Research Board, Department of Science & Technology, Government of India (Grant No. IPA/2021/000031). Pavithra K gratefully acknowledges the generous financial support and fellowship extended by the Department of Science and Technology, New Delhi, India, and the Anusandhan National Research Foundation (ANRF) (Grant No. IPA/2021/000031). The authors also thank the Central Instrumentation Facility at CSIR-CECRI Karaikudi for their assistance in providing characterization facilities.

Conflict of Interests

There are no conflicts to declare.

Data Availability Statement

The data that support the findings of this study are available in the supplementary material of this article.

Keywords: Li–O₂ batteries • Trimetallic spinel • Synergistic interaction • redox pairs • bifunctional ORR/OER • specific capacity

- [1] M. M. Thackeray, C. Wolverton, E. D. Isaacs, *Energy Environ. Sci.* **2012**, *5*, 7854–7863.
- [2] T. Liu, J. P. Vivek, E. W. Zhao, J. Lei, N. Garcia-Araez, C. P. Grey, *Chem. Rev.* **2020**, *120*, 6558–6625.
- [3] M. Balaish, J. W. Jung, I. D. Kim, Y. Ein-Eli, *Adv. Funct. Mater.* **2020**, *30*.
- [4] G. Girishkumar, B. McCloskey, A. C. Luntz, S. Swanson, W. Wilcke, *J. Phys. Chem. Lett.* **2010**, *1*, 2193–2203.
- [5] L. Liu, Y. Liu, C. Wang, X. Peng, W. Fang, Y. Hou, J. Wang, J. Ye, Y. Wu, *Small Methods* **2022**, *6*.
- [6] X. Lin, R. Yuan, S. Cai, Y. Jiang, J. Lei, S. G. Liu, Q. H. Wu, H. G. Liao, M. Zheng, Q. Dong, *Adv. Energy Mater.* **2018**, *8*, 1800089.
- [7] G. Karkera, S. G. Chandrappa, A. S. Prakash, *Chem. Eur. J.* **2018**, *24*, 17303–17310.
- [8] K. R. Yoon, K. Shin, J. Park, S. H. Cho, C. Kim, J. W. Jung, J. Y. Cheong, H. R. Byon, H. M. Lee, I. D. Kim, *ACS Nano* **2018**, *12*, 128–139.
- [9] S. Li, M. Wang, Y. Yao, T. Zhao, L. Yang, F. Wu, *ACS Appl. Mater. Interfaces* **2019**, *11*, 34997–35004.
- [10] K. Sun, J. Li, L. Huang, S. Ji, P. Kannan, D. Li, L. Liu, S. Liao, *J. Power Sources* **2019**, *412*, 433–441.
- [11] S. Guddehalli Chandrappa, G. Karkera, V. A. Gangadharappa, D. Chen, R. A. Caruso, P. Annigere S, *ACS Appl. Energ. Mater.* **2022**, *5*, 14680–14686.
- [12] J. Pan, X. L. Tian, S. Zaman, Z. Dong, H. Liu, H. S. Park, B. Y. Xia, *Batteries & Supercaps* **2019**, *2*, 336–347.
- [13] Q. Zhao, Z. Yan, C. Chen, J. Chen, *Chem. Rev.* **2017**, *117*, 10121–10211.
- [14] Z. P. Wang, J. H. Huang, L. Wang, Y. Y. Liu, W. H. Liu, S. L. Zhao, Z. Q. Liu, *Angew. Chem. Int. Ed.* **2022**, *61*, e202114696.
- [15] J. B. Goodenough, A. L. Loeb, *Phys. Rev.* **1955**, *98*, 391–408.
- [16] C. Wei, Z. X. Feng, G. G. Scherer, J. Barber, Y. Shao-Horn, Z. C. J. Xu, *Adv. Mater.* **2017**, *29*, 1606800.
- [17] L. An, Y. Hu, J. Li, J. Zhu, M. Sun, B. Huang, P. Xi, C. Yan, *Adv. Mater.* **2022**, *34*.
- [18] Y. Zhou, S. N. Sun, C. Wei, Y. M. Sun, P. X. Xi, Z. X. Feng, Z. C. J. Xu, *Adv. Mater.* **2019**, *31*, 1902509.
- [19] Y. Wu, H. Ding, T. Yang, Y. Xia, H. Zheng, Q. Wei, J. Han, D. L. Peng, G. Yue, *Adv. Sci.* **2022**, *9*, 2200523.
- [20] Y. J. Zhao, W. H. Tang, W. H. Liu, X. H. Kong, D. W. Zhang, H. Luo, K. W. Teng, R. P. Liu, *Small* **2023**, *19*, 2205532.
- [21] K. Song, L. Yuan, Z. Li, Y. Lv, B. Yang, Y. Yu, X. Shen, X. Hu, *Electrochim. Acta* **2020**, *353*, 136572.
- [22] C. Tomon, A. Krittayavathananon, S. Sarawutanukul, S. Duangdangchote, N. Phattharasupakun, K. Homlamai, M. Sawangphruk, *Electrochim. Acta* **2021**, *367*, 137490.
- [23] S. G. Mohamed, Y.-Q. Tsai, C.-J. Chen, Y.-T. Tsai, T.-F. Hung, W.-S. Chang, R.-S. Liu, *ACS Appl. Mater. Interfaces* **2015**, *7*, 12038–12046.
- [24] C. Huang, Y. Zhang, X. Li, H. Cao, Y. Guo, C. Zhang, *Appl. Catal. B* **2022**, *319*, 121909.
- [25] X. Ge, Y. Liu, F. W. T. Goh, T. S. A. Hor, Y. Zong, P. Xiao, Z. Zhang, S. H. Lim, B. Li, X. Wang, Z. Liu, *ACS Appl. Mater. Interfaces* **2014**, *6*, 12684–12691.
- [26] C. Li, X. Han, F. Cheng, Y. Hu, C. Chen, J. Chen, *Nat. Commun.* **2015**, *6*, 7345.
- [27] X. Chen, F. Han, X. Chen, C. Zhang, W. Gou, *Catalysts* **2022**, *12*, 1122.
- [28] M. K. Birhanu, M. Tsai, A. W. Kahsay, C. Chen, T. S. Zeleke, K. B. Ibrahim, C. Huang, W. Su, B. Hwang, *Adv. Mater. Interfaces* **2018**, *5*, 1800919.
- [29] H. Zhang, Y. Li, L. Zeng, Y. Pan, *Small* **2024**, *20*, 2307384.
- [30] T. Priamushko, E. Budiyanto, N. Eshraghi, C. Weidenthaler, J. Kahr, M. Jahn, H. Tuysuz, F. Kleitz, *ChemSusChem* **2022**, *15*, 202102404.
- [31] N. Fradette, B. Marsan, *J. Electrochem. Soc.* **1998**, *145*, 2320–2327.
- [32] J. Liu, J. Xie, R. Wang, B. Liu, X. Meng, X. Xu, B. Tang, Z. Cai, J. Zou, *Chem. Eng. J.* **2022**, *450*, 137961.
- [33] W. Cheng, Z. Wu, D. Luan, S. Zang, X. W. (David) Lou, *Angew. Chem.* **2021**, *133*, 26601–26606.
- [34] H. Cheng, M. L. Li, C. Y. Su, N. Li, Z. Q. Liu, *Adv. Funct. Mater.* **2017**, *27*, 1701833.
- [35] K. Song, W. Ai, Y. Zhang, Y. Zeng, Y. Yu, H. Qiao, Z. Liu, X. Shen, X. Hu, X. Hu, *J. Mater. Chem. A* **2021**, *9*, 3007–3017.
- [36] H. Wu, W. Sun, J. Shen, Z. Mao, H. Wang, H. Cai, Z. Wang, K. Sun, *ACS Sustainable Chem. Eng.* **2018**, *6*, 15180–15190.
- [37] H. Wang, F. Yin, N. Liu, H. Yu, T. Fan, B. Chen, *ACS Sustainable Chem. Eng.* **2021**, *9*, 4509–4519.
- [38] Y. Ren, J. Fan, Y. Fu, *Energy Mater.* **2023**, *3*, 300015.
- [39] S. Sun, Y. Sun, Y. Zhou, S. Xi, X. Ren, B. Huang, H. Liao, L. P. Wang, Y. Du, Z. J. Xu, *Angew. Chem.* **2019**, *131*, 6103–6108.
- [40] B. Talic, P. V. Hendriksen, K. Wiik, H. L. Lein, *Solid State Ionics* **2018**, *326*, 90–99.
- [41] A. N. Naveen, S. Selladurai, *Electrochim. Acta* **2014**, *125*, 404–414.
- [42] H. Park, B. H. Park, J. Choi, S. Kim, T. Kim, Y.-S. Youn, N. Son, J. H. Kim, M. Kang, *Nanomaterials* **2020**, *10*, 1727.
- [43] V. A. M. Brabers, F. van Setten, *J. Phys. D* **1983**, *16*, L169–L172.
- [44] J. Kossmann, M. L. Ortiz Sánchez-Manjavacas, H. Zschiesche, N. V. Tarakina, M. Antonietti, J. Albero, N. López-Salas, *J. Mater. Chem. A* **2022**, *10*, 6107–6114.
- [45] M. C. Biesinger, L. W. M. Lau, A. R. Gerson, R. St C Smart, *Appl. Surf. Sci.* **2010**, *257*, 887–898.
- [46] M. Thommes, K. Kaneko, A. V. Neimark, J. P. Olivier, F. Rodriguez-Reinoso, J. Rouquerol, K. S. W. Sing, *Pure Appl. Chem.* **2015**, *87*, 1051–1069.
- [47] J. Suntivich, H. A. Gasteiger, N. Yabuuchi, H. Nakanishi, J. B. Goodenough, Y. Shao-Horn, *Nat. Chem.* **2011**, *3*, 546–550.
- [48] S. G. Chandrappa, P. Moni, D. Chen, G. Karkera, K. R. Prakash, R. A. Caruso, A. S. Prakash, *J. Mater. Chem. A* **2020**, *8*, 20612–20620.
- [49] L. Li, X. Feng, Y. Nie, S. Chen, F. Shi, K. Xiong, W. Ding, X. Qi, J. Hu, Z. Wei, L.-J. Wan, M. Xia, *ACS Catal.* **2015**, *5*, 4825–4832.
- [50] E. Lee, J.-H. Jang, Y.-U. Kwon, *J. Power Sources* **2015**, *273*, 735–741.
- [51] P. Pramanik, S. Thota, S. Singh, D. C. Joshi, B. Weise, A. Waske, M. S. Seehra, *J. Phys. Condens. Matter* **2017**, *29*, 425803.
- [52] S. Ma, J. Wang, J. Huang, Z. Zhou, Z. Peng, *J. Phys. Chem. Lett.* **2018**, *9*, 3333–3339.
- [53] Y. Zhang, S. Zhang, M. Yuan, Y. Li, R. Liu, C. Nan, C. Chen, *Nano Res.* **2024**, *17*, 221–227.
- [54] P. Wang, C. Li, S. Dong, X. Ge, P. Zhang, X. Miao, R. Wang, Z. Zhang, L. Yin, *Adv. Energy Mater.* **2019**, *9*.
- [55] H. Wang, F. Yin, N. Liu, H. Yu, T. Fan, B. Chen, *ACS Sustainable Chem. Eng.* **2021**, *9*, 4509–4519.
- [56] S. Q. Ding, L. Wu, F. Zhang, X. X. Yuan, *Small* **2023**, *19*, 2300602.
- [57] L. L. Liu, C. C. Zhou, W. W. Fang, Y. Y. Hou, Y. P. Wu, *Energy Mater.* **2023**, *3*, 300011.
- [58] J. Wang, L. Ma, J. Xu, Y. Xu, K. Sun, Z. Peng, *SusMat* **2021**, *1*, 345–358.
- [59] K. M. Naik, *ACS Appl. Energ. Mater.* **2021**, *4*, 1014–1020.
- [60] D. Du, R. Zheng, X. Chen, W. Xiang, C. Zhao, B. Zhou, R. Li, H. Xu, C. Shu, *ACS Appl. Mater. Interfaces* **2021**, *13*, 33133–33146.

Manuscript received: October 16, 2024

Revised manuscript received: November 26, 2024

Accepted manuscript online: November 28, 2024

Version of record online: December 17, 2024